Target-based georeferencing of terrestrial radar images using TLS point clouds and multi-modal corner reflectors in geomonitoring applications

Journal Article

Author(s):
Schmid, Lorenz (ID); Medic, Tomislav (ID); Frey, Othmar (ID); Wieser, Andreas (ID)

Contents lists available at ScienceDirect

ISPRS Open Journal of Photogrammetry and Remote Sensing
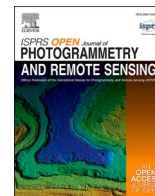
Target-based georeferencing of terrestrial radar images using TLS point clouds and multi-modal corner reflectors in geomonitoring applications

Lorenz Schmid [a,*], Tomislav Medic [a], Othmar Frey [b,c], Andreas Wieser [a]

[a] *Institute of Geodesy and Photogrammetry, ETH Zürich, Stefano-Franscini-Platz 5, 8093, Zürich, Switzerland*
[b] *Institute of Environmental Engineering, ETH Zürich, Laura-Hezner-Weg 7, 8093, Zürich, Switzerland*
[c] *Gamma Remote Sensing, Worbstrasse 225, 3073, Gümligen, Switzerland*

ARTICLE INFO

ABSTRACT

Terrestrial Radar Interferometry (TRI) is widely adopted in geomonitoring applications due to its capability to precisely observe surface displacements along the line of sight, among other key characteristics. As its deployment grows, TRI is also increasingly used to monitor smaller and more dispersed geological phenomena, where the challenge is their precise localization in 3d space if the pose of the radar interferometer is not known beforehand. To tackle this challenge, we introduce a semi-automatic target-based georeferencing method for precisely aligning TRI data with 3d point clouds obtained using long-range Terrestrial Laser Scanning (TLS). To facilitate this, we developed a multi-modal corner reflector (mmCR) that serves as a common reference point recognizable by both technologies, and we accompanied it with a semi-automatic data-processing pipeline, including the algorithms for precise center estimation. Experimental validation demonstrated that the corner reflector can be localized within the TLS data with a precision of 3–5 cm and within the TRI data with 1–2 dm. The targets were deployed in a realistic geomonitoring scenario to evaluate the implemented workflow and the achievable quality of georeferencing. The post-georeferencing mapping uncertainty was found to be on a decimeter level, matching the state-of-the-art results using dedicated targets and achieving more than an order of magnitude lower uncertainty than the existing data-driven approaches. In contrast to the existing target-based approaches, our results were achieved without laborious visual data inspection and manual target detection and on significantly larger distances, surpassing 2 km. The use of the developed mmCR and its associated data-processing pipeline extends beyond precise georeferencing of TRI imagery to TLS point clouds, allowing for alternatively georeferencing using total stations, mapping quality evaluation as well as on-site testing and calibrating TRI systems within the application environment.

1. Introduction

Ground-based or terrestrial radar interferometry (TRI) can provide line-of-sight displacement observations with millimeter-level precision and is often used for monitoring large-scale structures such as bridges, dams, and towers. Additionally, it is widely adopted in geomonitoring of landslides, mines, and glaciers (Monserrat et al., 2014; Caduff et al., 2015; Pieraccini and Miccinesi, 2019). Its capability to identify small displacements over large areas, its high temporal resolution (1–2 min), along with the possibility of providing observations under challenging atmospheric conditions, makes it a suitable tool for early warning systems (Agliardi et al., 2013). In this context, precise localization and detailed mapping of observations are not so crucial for interpreting the

results, as the primary focus is on detecting any movements and their acceleration rates for further decision-making (Eberhardt et al., 2008). Conversely, TRI systems are now more frequently used to also monitor and observe smaller and scattered geological phenomena, such as rockfalls (Frodella et al., 2016; Kos et al., 2010). A major challenge in these scenarios is accurately determining the initial locations of rockfalls (Crosta and Agliardi, 2003). These locations are important for rockfall modeling and process understanding (Rossi et al., 2021). One way to tackle the challenge is to project the 2d displacement maps obtained by TRI onto 3d surface models. This allows relating calculated displacements to the real world and facilitates subsequent interpretation of the TRI results (Li et al., 2019).

Combining the 2d displacement maps and 3d surface models

typically involves mapping in two steps. The first one is to georeference the TRI instrument to a 3d surface model. This step is also referred to as rigid registration or alignment, and it entails estimating the position and orientation of the TRI instrument's coordinate system in terms of a rigid transformation (3 translations, 3 rotations) relative to the surface model. Georeferencing is a mandatory prerequisite for the second step, i.e., geocoding. Within this step, the information of each pixel of the displacement maps is assigned to the corresponding areas within the 3d surface model. Under certain conditions—such as the absence of layover and significant surface discontinuities—these areas may be contiguous and sufficiently small to be considered a single, well-defined position. In such cases, geocoding accurately relates each individual pixel from the TRI image to that specific position. Geocoding needs to take the specific imaging processes of the deployed radar system, the radar data processing, and the detailed topography into account. In this study, we focus on enhancing georeferencing quality, which in turn facilitates more accurate geocoding.

The difficulty in georeferencing the TRI data relative to 3d surface representations, such as terrestrial laser scanning (TLS) point clouds, lies in the absence of clearly identifiable natural features that can be used for establishing direct correspondences, the significant imbalance of data resolution between the data sources, as well as in the imaging process of the respective deployed TRI system type, particularly in case of a synthetic aperture, see, e.g. Schmid et al. (2023). Currently, various approaches are being developed for georeferencing to tackle the above challenges. A straightforward approach involves directly determining the position and orientation of a radar instrument through a topographic survey. However, Noferini et al. (2006) and Rebmeister et al. (2022) have pointed out that even minor and unavoidable orientation inaccuracies, on the order of a few tenths of a degree, can significantly impair the mapping accuracy and lead to geocoding errors which surpass the level of the radar image resolution.

As an alternative, Noferini et al. (2006) proposed a data-driven approach that uses a coarse Digital Elevation Model (DEM) generated from the radar observations themselves, where the transformation parameters are estimated by minimizing the distances between such a DEM and a reference 3d surface model. However, this approach is not applicable to all TRI systems. Schmid et al. (2023) proposed another data-driven method relying on approximate correspondences between natural features identified in TRI amplitude images and the angles of incidence estimated from a 3d point cloud. Although the authors demonstrated high mapping precision on a single use case, the transferability and the absolute accuracy have yet to be verified.

Common disadvantages of such data-driven methods are that: a) the resulting quality highly depends on the terrain configuration and natural features found on-site, and b) there is a lack of established approaches for quantitative assessment of georeferencing quality. These disadvantages are addressed by the approaches relying on artificial targets, e.g. corner reflectors (CRs), pre-installed in the region of interest.

Caduff and Rieke-Zapp (2014) demonstrated georeferencing for distances up to 1 km using standard CRs. They aligned the TRI data with an up-to-date photogrammetrically reconstructed 3d model acquired concurrently with the radar observations and achieved georeferencing with deviations of several decimeters. However, fine alignment with the 3d model required substantial manual work to identify and precisely localize the CRs in both datasets. Comparably, Wujanz et al. (2013) investigated georeferencing of TRI data with TLS point clouds using standard CRs. Their approach consisted of estimating the centers of the CRs by finding the intersection point of the CR plane surfaces identified in the TLS point clouds and by finding local maxima in the TRI amplitude image. Although they showed the method to be efficient, its application is limited to close range (demonstrated up to 50 m) due to the unfavorable relationship between common CR sizes and the laser beam diameter at large distances. To enhance the visibility at longer ranges, Zheng et al. (2018) boosted the reflectivity of the CRs for TLS by adding a reflective foil at their center. However, even with this

adjustment, the approach was only applicable at comparably close ranges, as the center of the CR would no longer be detectable in TLS point clouds beyond these distances because of the laser beam divergence.

To summarize, the approaches described in the literature to date exhibit one or multiple of the following characteristics: insufficient precision for tasks demanding high localization quality; lacking established quality estimation strategies; non-controllable quality depending on the on-site situation and availability of natural features; lack of automation; not useable at larger distances.

Herein, we introduce a georeferencing method that addresses these challenges. It is a semi-automated, target-based method for precisely aligning TRI data with TLS point clouds, primarily developed for long-range geomonitoring applications with sufficient terrain accessibility. Beyond georeferencing, the expected use cases for the method are mapping quality assessment and establishing ground truth for the further development of data-driven georeferencing methods. The approach utilizes multi-modal CRs designed specifically for this purpose, and a specific data processing pipeline developed herein, as well. We demonstrate the applicability in a realistic geomonitoring setting with distances over 2 km, and we augment the demonstration with a comprehensive evaluation including the target center estimation precision, the variability of transformation parameters, and the resulting mapping error.

The article is organized as follows: In section 2 we introduce the methodology, including the design of the proposed reflectors, the semi-automatic pipeline for detecting and estimating target centers in both TRI and TLS data, and the georeferencing process. Section 3 covers the experiments for investigating the quality of target center estimation and georeferencing. Conclusions and an outlook are presented in Section 4.

2. Methods

This section describes our design and development of the multi-modal corner reflector (mmCR), the newly developed algorithms for locating the CR within the TLS point clouds and the radar images, and the accompanying algorithmic pipeline for georeferencing of TRI images with the TLS point clouds.

2.1. Multi-modal corner reflector

We posed the following criteria for the design of the mmCR:

- The mmCR materializes a common distinct point which is relatively easy to detect within the data of both technologies (TRI and TLS) and facilitates semi-automatic data processing.
- The coordinates of the materialized point must be well-defined and can be estimated within each data set with sufficient precision for georeferencing.
- The mmCR can be oriented as needed, mounted stably on various surfaces, and is sufficiently robust with respect to challenging weather conditions.
- It has to be compact and lightweight for ease of transportation.

In the following text, we explain how we ensured that those criteria were met. Our design of the mmCR primarily relies on a combination of target designs already applied for each technology individually.

Dedicated corner reflectors or targets for radar (incl. TRI) are designed in several shapes to suit specific applications, such as establishing geometric and radiometric reference points, aiding georeferencing, as well as mitigating atmospheric phase screen (APS) and other factors affecting the interferometric phase (Luzi et al., 2004). In geomonitoring applications, they are typically realized as trihedral CRs, defined by three orthogonal surfaces. The triangular trihedral CR, composed of three equal right-angled isosceles triangles, is the most commonly deployed type of CR for both satellite and ground-based

remote sensing systems due to the following characteristics: ease of construction, mechanical robustness, lighter weight compared to other shapes (Garthwaite, 2017).

Another relevant, if not the most critical, design characteristic is the radar cross section (RCS), often denoted as σ. It defines how well an object is detectable by the radar, with a larger RCS being preferable. The triangular trihedral CR has a smaller RCS compared to, e.g., a square trihedral CR with equal length of the orthogonal edges (Ruck, 1970). However, the triangular design offers greater tolerance in CR alignment relative to the instrument as it tolerates a wider deviation angle from the symmetry axis (boresight) before experiencing a significant reduction in RCS, and therefore in signal-to-clutter ratio (SCR). For example, for triangular CR the 3 dB beamwidth reduction occurs at an angle of around 40°, whereas the square CR experiences the same reduction already at an angle of 23° (Ruck, 1970). This attribute makes the triangular CR preferable for field setups, where precise alignment might be challenging. Therefore, we adopted the triangular CR design for our mmCR.

For georeferencing TLS scans, targets are typically utilized. They can be separated into two categories. The first one comprises targets with diffusely reflecting surfaces, whose geometrical shape or reflectivity pattern represents the marked point. To assure precise target center estimation (TCE), i.e., determination of the coordinates of the marked point within the point clouds, these targets have to be sampled by a sufficiently high number of points ($>$100) representing the geometric shape (e.g., a sphere) or reflectivity pattern (e.g., a planar checkerboard). Because of the beam divergence, i.e., nearly linear increase of beam diameter with distance, such targets would have to be very large at large distances, resulting in stability issues and logistic challenges. Targets of this type are thus commonly used over shorter ranges of up to about 100 m only, and are unsuitable for long-range geomonitoring.

The second category consists of targets with retro-reflective surfaces. This characteristic ensures that even if only a small part of the laser beam hits the target, the resulting measurement can still be informative enough to aid in estimating the target's center. Such targets can be realized as, e.g., flat or cylindrical targets covered by reflective foil (Pesci and Teza, 2008; Wilkes et al., 2017). Also, retro-reflective glass prisms, widely used for geodetic measurements, have been applied successfully to TLS registration, see e.g., Schröder and Gaisecker (2022), and geomonitoring, see e. g, Winiwarter et al. (2023); Schröder et al. (2022). It should be verified that the TLS intended to be used is compatible with retro-reflective glass prisms, as specified by the manufacturer, to avoid any potential damage or measurement inaccuracies.

Therefore, we propose the mmCR as a combination of a triangular trihedral CR and a retroreflective glass corner cube prism mounted to share their respective vertices, as depicted in Fig. 1. The common vertex is the back-scattering center for both measurement systems and thus the materialized reference point. As the uncertainty of the target center estimation from TRI images is an order of magnitude higher than the expected errors in aligning the prism with the exact CR center, we consider them to be perfectly, providing a common distinct point in the data (1st design condition).

The next design choice requiring consideration is the right size of both mmCR elements, where it is necessary to optimize two conflicting goals, sufficient SCR and a compact form. Due to a) strong retro-reflective properties of the glass prism in the TLS scanner working wavelength ranges, b) sufficient scanning resolution, and c) large laser beam footprint at large distances, the prism can be relatively small compared to the CR and still assure sufficient number and quality of TLS measurements for precise center estimation (Schröder and Gaisecker, 2022). Hence, we relied on off-the-shelf 1-inch glass corner cube prisms that can fit into the CR, narrowing our focus to only the size requirements dictated by the specific needs of the TRI system.

For that, we adopted the method outlined by Garthwaite (2017) regarding the design of radar CRs. The required target size depends on
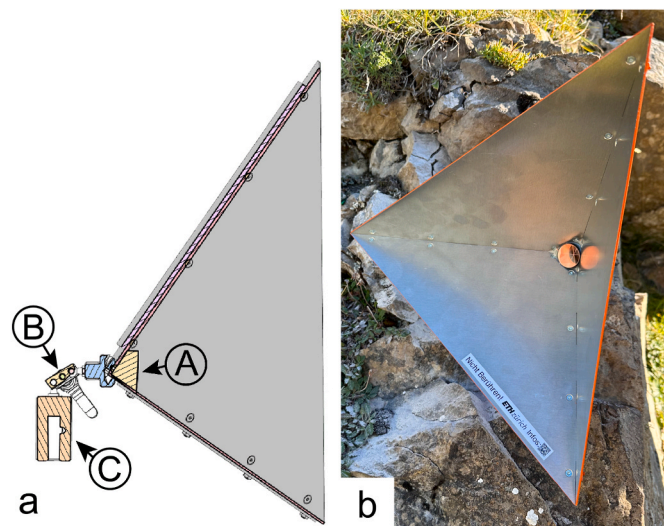

Fig. 1. Vertical cross-section (a) and front view (b) of the mmCR, with prism (A) at the vertex of the CR, a spherical dual ball head joint (B) for enabling alignment, and mount (C) to connect to a standard survey bolt for stable setup.

multiple factors, including the center frequency of the radar system, the expected angle of incidence, the necessary opening angle (expressed as the 3 dB beamwidth), and the expected surrounding clutter, as discussed by Garthwaite et al. (2015). Ideally, for high-quality georeferencing, we would strive to minimize the error in 3d position of the estimated CR center. However, due to the lack of a comprehensive body of literature on the topic, we rely on the established line-of-sight (LOS) displacement error as the specific metric for determining the CR size. The LOS displacement error is proportional to the effective phase error φ_{err}, which in turn is inversely proportional to the *SCR*. The *SCR* is the ratio between the theoretical peak (maximum) RCS value of the CR σ_T and the averaged background clutter $\langle \sigma_0 \rangle$ of the surrounding environment (Freeman, 1992)

$$SCR = \frac{\sigma_T}{\langle \sigma_0 \rangle} \tag{1}$$

By considering the expected background clutter $\langle \sigma_0 \rangle$ and the maximal acceptable LOS displacement error, the required σ_T can be computed. As σ_T is related to the non-hypotenuse side of the triangular plates a and the wavelength of the center frequency of the TRI λ by the following expression:

$$\sigma_T = \frac{4\pi a^4}{3\lambda^2} \tag{2}$$

we can use this relationship to estimate the required size of the CR. In our work, we computed the needed size a for the TRI with the wavelength $\lambda = 17.4$ mm (corresponding to a center frequency of 17.2 GHz, typical for TRI systems), a -5 dB background clutter $\langle \sigma_0 \rangle$, which is typical for mountains (Nathanson et al., 2004, p. 332), and a LOS displacement error of 0.1 mm specified in Garthwaite (2017). These considerations yielded a side length a of approx. 25 cm which we adopted for our mmCR. The finalized design fulfills the 1st and 4th design criteria, while the other two points still have to be assured.

Although the selected triangular CR offers higher tolerance in aligning the target face relative to the instrument compared to other target types, achieving sufficiently precise alignment is still required. To facilitate this, we incorporated a spherical dual ball head joint (indicated as B in Fig. 1a) to connect the mmCR and the mount (marked as C) for the geodetic survey bolt. This allows full 6 degrees of freedom (DOF), simplifying the aiming of the target face towards the instruments. To support the aiming, we developed a custom 3d-printed mounting system to attach a telescopic sight on top of the mmCR, as shown in Fig. 2. The

Fig. 2. Installed mmCR with the 3d-printed mounting system for attaching the telescopic sight.

mount aligns the optical target axis parallel to the antenna boresight, giving us the possibility to aim the mmCR with 0.5°–1° uncertainty (magnification dependent) toward the instrument, based on the specification of the telescope and experimental assessment. Deploying this system ensures fulfillment of the 3rd design criterion. Only the 2nd criterion was not directly addressed during the construction phase of the mmCR but was instead experimentally validated, as described in Sec. 3.

2.2. Pipeline

The implemented data processing pipeline is depicted in Fig. 3. In subsequent sections, we first address the target detection and center estimation for TLS in Sec. 2.2.1 (block A in Fig. 3), and for TRI in Sec. 2.2.2 (block C). The georeferencing workflow, detailed in Sec. 2.5, utilizes the 3D coordinates of targets identified in TLS point clouds and 2D coordinates of targets identified in TRI images to establish a correspondence between the 2D TRI images and the 3D model (point cloud).

It is worth noting that here we use the term 'georeferencing,' to describe relating hardly-interpretable 2D TRI digital raster images to 3D point clouds. This allows relating TRI data to real-world geological features and formations, which is necessary for interpreting the observed displacements (see Sec. 1). Hence, in this case, georeferencing does not necessarily involve alignment to a global coordinate system, but rather to any coordinate system in which the TLS point cloud is represented.

2.2.1. Target detection and center estimation for TLS

For the integrated target detection and center estimation of individual targets in the TLS point cloud data, we adapt the approach described by Schröder and Gaisecker (2022) for detecting the centers of

glass prisms. The target center detection starts by selecting the point $\mathbf{p}_{max} \in \mathbb{R}^3$ with the highest intensity of the reflected laser beam I_{max} in the point cloud of the monitored region. This point is the center for a radial neighborhood subset $\mathbb{M}$, defined as $\mathbb{M}(\mathbf{p}_{max}) = \{\mathbf{q} \in \mathbb{R}^3 \mid \|\mathbf{q} - \mathbf{p}_{max}\|_2 < r\}$ consisting of all points $\mathbf{q}$ that lie within a predefined spherical neighborhood of radius r, where the distance between any point $\mathbf{q}$ and $\mathbf{p}_{max}$ is measured using the Euclidean norm.

In our approach, we calculate radius r based on the known laser beam divergence angle and measured distance to $\mathbf{p}_{max}$ and we multiply it by a semi-randomly chosen factor of 20 to guarantee that the neighborhood is sufficiently large to encompass all points partially hitting the target. It can be assumed that all measured points sampling the mmCR should lie on a common plane (Winiwarter et al., 2023), where small discrepancies from this assumption occur due to measurement uncertainties. This assumption is leveraged both for outlier removal and subsequent center estimation. For the outlier removal, we implemented a plane fit using the robust M-Estimator Sample Consensus (MSAC) algorithm and kept only points that lie within a predetermined distance threshold d_P from this plane. As a threshold, we chose three times the range standard deviation as specified by the manufacturer. Fig. 4 illustrates the outcome of this process, showing the filtered subset of points $\mathbb{M}_f$ colored by the intensity. At this stage, we have implemented an additional outlier removal mechanism for identifying eventual false mmCR detections due to simple I_{max} criterion. We placed a threshold for the minimal acceptable $\mathbb{M}_f$ value (set to 100). The $\mathbb{M}_f$ below this value indicates a false target, points $\mathbb{M}_f$ are in this case deleted from the point cloud, and the whole target detection is repeated.

Based on the resulting $\mathbb{M}_f$, dimensionality reduction via principal component analysis (PCA) is performed to project the remaining 3d points onto the aforementioned virtual plane for the target center estimation step, which is based on image-correlation and requires all intensity values to be projected onto a common plane.

We first center the data, where for each point $\mathbf{q}_i$, we compute the adjusted coordinates, $\mathbf{Q}'$ by:

$$\mathbf{Q}'_i = \mathbf{q}_i - \boldsymbol{\mu}, \quad \text{for } i = 1, \ldots, N \tag{3}$$

where $\mathbf{q}_i$ represents the 3d coordinate values of the ith point, $\boldsymbol{\mu}$ is the mean in all three dimensions, and N is the total number of points.

Following, the Single Value Decomposition (SVD) is performed:

$$\mathbf{Q}' = \mathbf{U}\boldsymbol{\Sigma}\mathbf{V}^T \tag{4}$$

where $\boldsymbol{\Sigma}$ is a matrix containing the singular values, and $\mathbf{U}$ contains the transformed point coordinates in the principal component space spanned by $\mathbf{V}$. The dimensional reduction is practically realized by retaining only the first two columns of the matrix $\mathbf{U}$, containing coordinates $[u_i, v_i]$ for each point. This sequence of operations effectively translates the point cloud to a target-centric coordinate system, rotates it so that the z-axis coincides with the normal direction of the aforementioned virtual plane, and, finally, discards this 3rd dimension, which is redundant for the following target center estimation step. The relationship between the 3d and the reduced 2d points is presented in Fig. 4.

From these 2d points, the target centers are estimated as the locations where the intensity values reach their maximum. To facilitate the target center estimation with a precision better than the original scanning resolution, we used a 2d Gaussian fit that incorporates intensity I as the third dimension, as a smart interpolation technique (illustrated in Fig. 5). The Gaussian function is used as it well approximates the laser beam footprint, see e.g. Reshetyuk (2009), and the fitting is realized by employing a nonlinear least squares algorithm. The 2d center of the Gaussian fit, denoted by $\mathbf{s}_{2D,TLS} = [u_c, v_c]$, is the estimated (interpolated) point of maximal intensity $\tilde{I}_{max}$, and is subsequently back-projected into 3d as

$$\mathbf{s}_{TLS} = [\, u_c \quad v_c \quad 0\,]\mathbf{V} + \boldsymbol{\mu} \tag{5}$$
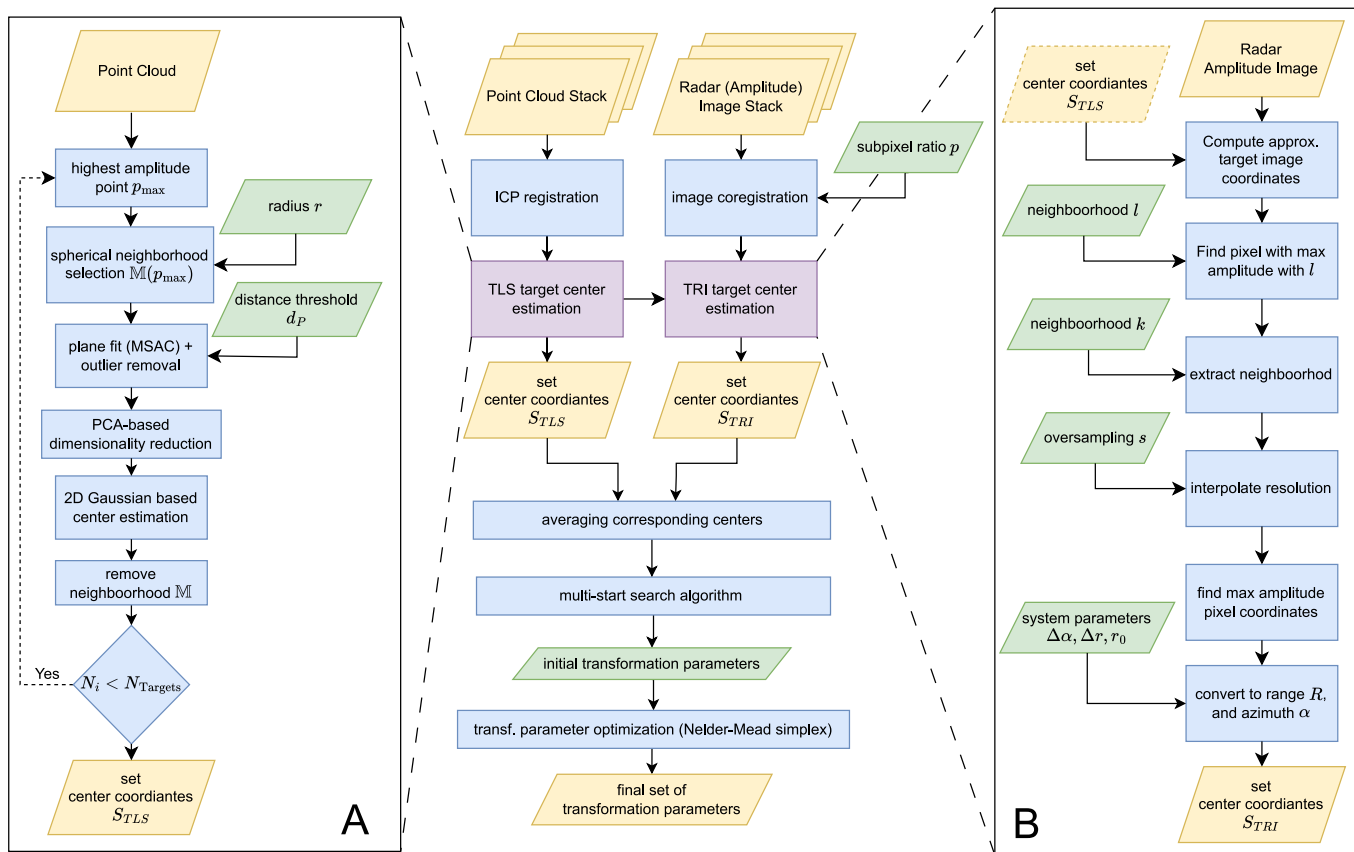
Fig. 3. Automated processing pipeline for target detection and center estimation (TCE) in the TLS point clouds and TRI images with the subsequent georeferencing based on the estimated centers. (A) marks the TCE for each detected mmCR in the TLS point clouds, which are then used in the TCE for the TRI images (B) as approximate coordinates.
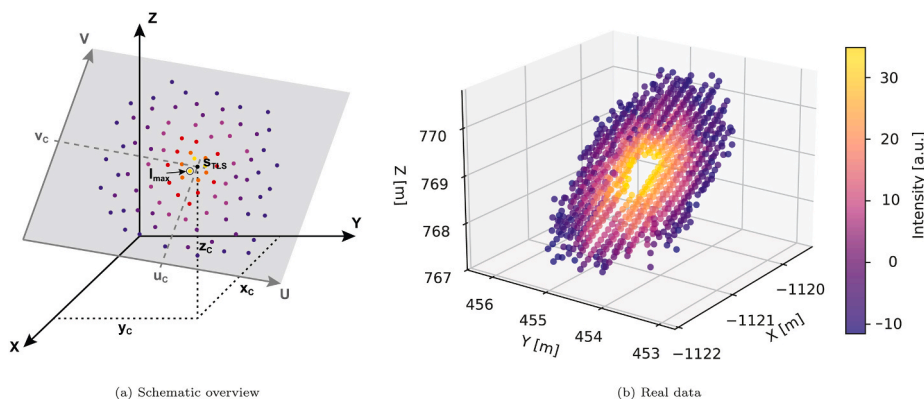

Fig. 4. (a) Schematic overview of the filtered subset of points $\mathbb{M}_f$, the estimated plane defined by the 1st and 2nd principal components, and the relation between the estimated 2D center $\mathbf{s}_{2D,TLS} = [u_c, v_c]$ and the position $\mathbf{s}_{TLS}$ in the 3D Cartesian system. (b) Visualization of the filtered subset of points from a measured prism, with each point color-coded according to its intensity value. (For interpretation of the references to color in this figure legend, the reader is referred to the Web version of this article.)

Following the detection and center estimation for the first target, the selected neighborhood $\mathbb{M}$ is excluded from the point cloud of the monitored scene. The entire procedure is iteratively performed, as illustrated in Fig. 3, until the specified number of installed targets $N_{Targets}$ is detected and their centers are estimated. The outcome of the process is a collection of 3d target center coordinates $\mathbf{S}_{TLS}$. The described data processing is designed to be generally applicable and adaptable for any particular TLS system configuration.

2.2.2. Target detection and center estimation for TRI

The target detection and center estimation for TRI relies on the amplitude images derived from Single Look Complex (SLC) images. In the initial step, the previously estimated 3d target coordinates $\mathbf{S}_{TLS}$ are converted into range and azimuth coordinates corresponding to the SLC image and the assumption that the TLS and TRI instruments are located at approximately the same position and leveled (typical set-up). This assumption allows us to roughly map the position of the targets into the TRI space with just the azimuth angle between the two systems as an
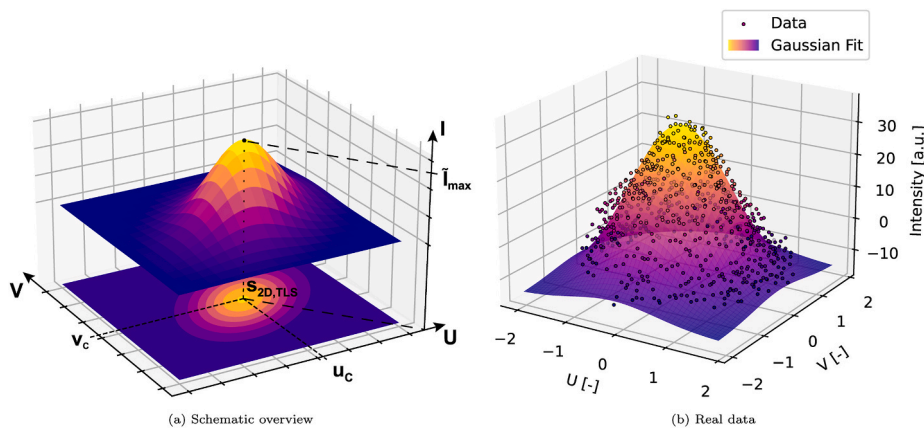
Fig. 5. (a) Schematic representation of the 2D Gaussian fitting process, where the intensity I serves as the third dimension. The peak of the Gaussian fit, $\tilde{I}_{max}$, represents the estimated target center, with the corresponding coordinates u_c and v_c derived from this peak. (b) Application of the 2D Gaussian fit on real-world data, illustrating the fit to a point cloud of a measured prism. The data points (black dots) are overlaid with the Gaussian fit surface (color gradient) to visualize the alignment between the model and the actual measurements. (For interpretation of the references to color in this figure legend, the reader is referred to the Web version of this article.)

unknown variable. To find the approximate azimuth angle, an iterative search is performed.

First, for each target, a neighborhood of l pixels, centered around these approximately mapped coordinates, is extracted and within this neighborhood, the pixel exhibiting the highest amplitude is selected. This process is then repeated, adjusting the azimuth of the targets by one azimuth pixel ($\Delta\alpha$) at a time until the entire SLC image is searched through. Ultimately, the coordinates with the respective azimuth angle are selected as the approximate centers, where the sum of the amplitudes over all targets reaches the maximum.

The neighborhood size l must be larger when the deviation from the assumption that TLS and TRI instruments are in immediate proximity is bigger. For our experiments, we identified $l = 30$ as effective through iterative testing. If the positions of the two instruments are significantly different (e.g. more than 10 m apart) and other highly reflective objects are present in the scene (like poles or power lines), this automatic target detection can become error-prone. In this case, estimating the positions of mmCRs in TRI images have to be supported by visual inspection and eventual manual selection, resulting in a semi-automatic georeferencing approach. The analysis of the breaking point of the implemented automatic target detection is out of the scope of this work.

Subsequently, the center estimation is done for all identified targets as follows. A square neighborhood of k pixels in each direction from the approximate target center is selected in the amplitude image, with k being heuristically determined as 5 for our specific application. For the precise center estimation, this 11x11 matrix is oversampled by zero-padding with s pixels (in our case, 200 pixels) in Fourier space, as described by Czikhardt et al. (2021). Within this oversampled matrix, the signal peak is identified by locating the pixel with the maximum amplitude, resulting in the sub-pixel precise position $[n, m]$ (row and column-wise) within the original amplitude image.

An alternative approach for precise center estimation could be to fit a function, such as a lower-degree polynomial, 2d Gaussian (as shown in 2.2.1 for TLS), or a custom function that potentially incorporates factors like the antenna pattern and specific processing characteristics. We compared these alternatives to the described approach, but there were no significant differences. Hence, we opted for the maximum-based detection due to computational efficiency.

Following the identification of the signal peak in the image coordinate system, the image coordinates are converted into metric space by considering the specific parameters of the radar system. The mapping for a ground-based synthetic aperture radar (GB-SAR) is discussed, e.g., by Schmid et al. (2023). For the system deployed in this work, the range and azimuth for the target i are determined using the following relations:

$$\alpha_i = n \times \Delta\alpha, R_i = m \times \Delta r + r_0 \tag{6}$$

Here, the pixel index values n, m are scaled by the azimuth ($\Delta\alpha$) resp. range resolution (Δr). Additionally, the range equation incorporates a range offset r_0 to compensate for a minimum range measurement threshold, i.e. offset, set by the operator during data acquisition, as e.g. 30 m for our experiments. These polar coordinates are then converted into metric target coordinates $\mathbf{c}_{TRI}$ by:

$$\mathbf{s}_{TRI} = [R_i\cos(\alpha_i), R_i\sin(\alpha_i)] \tag{7}$$

The target center estimation and detection are done for all target locations provided by the TLS dataset, which results in the collection of $N_{Targets}$ TRI target centers $\mathbf{S}_{TRI}$ (Fig. 3, B).

2.2.3. Georeferencing

Building on the target detection and center estimation outlined for both technologies in the previous section, this section introduces the workflow for georeferencing (Fig. 3).

In this step, our goal is to first coarsely estimate and then refine the transformation, linking the corresponding sets of targets $\mathbf{S}_{TLS}$ and $\mathbf{S}_{TRI}$ in both coordinate systems. We treat the TLS data as error-free or given variables to avoid the singular solution during the estimation. This assumption is based on their superior range and angular resolution relative to TRI systems, and on a small preliminary analysis, in which we compared the TLS and geodetic-grade total-station measurements (acquired with a Leica Total Station TS60) and noted a strong agreement between the measured distances within about 5 mm (after appropriate transformations and meteorological corrections), confirming the high quality of TLS observations.

During the assessment of the target center estimation precision (Sec. 3.1), we demonstrated an improvement in the precision by averaging, when multiple data acquisitions were available. However, to benefit from such averaging, it was necessary to first align (register) each dataset to a common reference epoch due to the instrument setup instability during data acquisition (Janßen et al., 2021). Because of these observations, we introduced this "registration and averaging of the original TLS and TRI observations" step as a part of our standard georeferencing workflow, performed before target center detection and estimation, as outlined in Fig. 3. For aligning the series of TLS point clouds, we employ the point-to-point Iterative Closest Point (ICP) algorithm (Besl and McKay, 1992) and for the series of TRI images, we use the subpixel image registration algorithm based on amplitude information, as the one described in Guizar-Sicairos et al. (2008).

The georeferencing equation is based on a seven-parameter trans-

formation that incorporates a 6 Degrees of Freedom (6DOF) model, including translation $\mathbf{T} = \begin{bmatrix} T_x, T_y, T_z \end{bmatrix}$ and rotation parameters ω, ϕ, and γ (Euler angles) that form the rotation matrix $\mathbf{R} = \mathbf{R}_Z(\omega)\mathbf{R}_Y(\psi)\mathbf{R}_X(\gamma)$, plus an additional range bias δr for the TRI data. The rationale and consequences of incorporating this range bias term are further discussed in Sec. 3.5.

We would like to mention, that we do not account for a prism constant term for the TLS observations during georeferencing. In the current setup, any discrepancies attributable to the prism constant will be absorbed by the range bias term introduced for the TRI. However, suppose the mmCR is used alongside a geodetic network, which utilizes total station or GNSS coordinates for superior accuracy. In that case, it is advisable to consider the prism constant given by the manufacturer or estimate its value experimentally before implementation.

For both coarse estimation and refinement steps, the objective is to minimize the cost function, defined as the L_2-norm between $\mathbf{S}_{TRI}$ and $\mathbf{S}_{TLS \to TRI}$, where $\mathbf{S}_{TLS \to TRI}$ is the projection of 3d $\mathbf{S}_{TLS}$ into the 2d TRI related coordinate system.

For that, $\mathbf{S}_{TLS}$ must first be aligned with the TRI system's orientation and position, ensuring they match the radar system's reference frame, by

$$\mathbf{S}'_{TLS} = \mathbf{S}_{TLS}\mathbf{R}^T + \mathbf{T} \tag{8}$$

Subsequently, these transformed 3d coordinates are projected into the radar image to obtain their 2d representations. In our experiment, which employs a real aperture radar (RAR) system, the 2d coordinates $\mathbf{S}_{TLS \to TRI}$ are derived by

$$\mathbf{S}_{TLS \to TRI} = \begin{bmatrix} R_{TLS,i}\cos\alpha_i, R_{TLS,i}\sin\alpha_i \end{bmatrix} \tag{9}$$

Here, $R_{TLS,i} = \sqrt{x_i^2 + y_i^2 + z_i^2}$ represents the radial distance of each target center from the TLS scanner origin, and $\alpha_i = \tan^{-1}(\frac{y_i}{x_i})$ the azimuth angle. For experiments utilizing a synthetic aperture radar (SAR) system, a different set of mapping equations is required (Schmid et al., 2023).

For the coarse parameter estimation, we employ the multi-start search algorithm (Ugray et al., 2006), which systematically explores the wide parameter search space by sampling diverse starting points. We limited the search space for some parameters by defining bounds to reduce computation time. In our case, we limited the rotations for $\mathbf{R}_Y(\psi)$ and $\mathbf{R}_X(\gamma)$ to $\pm 10°$, assuming that the instrument is set up horizontally and approximately leveled, which is a generalizable assumption for the majority of TRI systems and experiments. Subsequently, the parameter estimates are refined through local optimization employing the Nelder-Mead simplex method (Lagarias et al., 1998). While the chosen algorithms have demonstrated effectiveness and efficiency in application, alternative global and local optimization techniques could be employed to achieve similar or better georeferencing results. However, conducting a comprehensive comparison to determine the most effective combination of algorithms falls beyond the scope of this work.

3. Experiments

This section describes the investigations of the target center estimation (TCE) precision for the proposed mmCR and of the achievable georeferencing uncertainty in two separate experiments. The experiment set-ups are described in Sec. 3.1 and 3.4, while the corresponding results are presented in 3.2, 3.3 and 3.5.

3.1. TCE precision: experiment set-up

In the first experiment, we evaluate the TCE precision with mmCR for both TRI and TLS systems. The experiment was conducted in an open and predominantly flat terrain near Rothenthurm, SZ, Switzerland (Fig. 6) to provide clear observational capabilities over large distances that would also be encountered in geomonitoring practice. We deployed the real aperture radar GPRI-II (Werner et al., 2012; Strozzi et al., 2012)
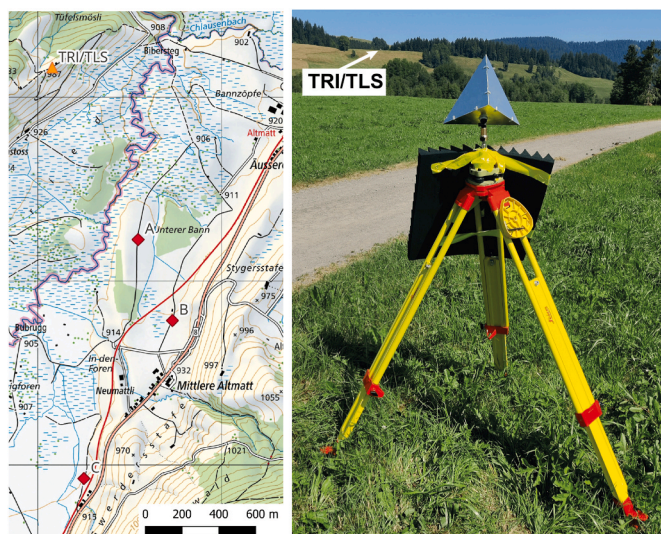

Fig. 6. The map (left) gives an overview of the experimental setup, while the positions (rhomboids A, B, and C) represent the location of the mmCR targets and the orange triangle the position of the instruments. The mmCR were set up at each position as depicted on the right. Basemap: ⓒ swisstopo. (For interpretation of the references to color in this figure legend, the reader is referred to the Web version of this article.)

from Gamma Remote Sensing AG, alongside a Riegl VZ-4000 long-range TLS scanner. Most relevant instrument specifications are listed in Table 1. Both instruments were positioned side by side on a ridge, providing an unobstructed view up to a distance of 2500 m. They were set up on heavy-duty surveying tripods, leveled using a bubble level, and operated remotely so that the measurements remained unaffected by eventual vibrations caused by the operator's motion.

We positioned the mmCR at three distinct distances (1.2, 1.5, and 2.3 km), spanning a range typical in long-range geomonitoring to investigate if the achievable TCE precision is influenced by distance. These locations are marked as points A, B, and C in Fig. 6 (left). The mmCR was mounted on a surveying tripod, with all metallic parts close to the mmCR covered with microwave-absorbing foam (also used in anechoic chambers), as shown in Fig. 6 (right), to minimize interference of backscatter from these parts with the backscatter from mmCR. Additionally, the placement of the targets was carefully selected to ensure they were predominantly surrounded by pasture, a measure taken to minimize strong reflections from the surrounding environment to be able to assess the TCE precision in the "near ideal" conditions, while the relationship of these precision estimates with real application cases is analyzed in Sec. 3.5.

The measurement program for each mmCR position included 14 sequential TLS observations as a trade-off between available time and a sufficient number of repetitions for calculating reliable statistical estimates. Each scan took about 3 min, for a point cloud with a field of view of 6° horizontally x 4° vertically. For the TLS, we selected an angular resolution of 0.0045°, corresponding to half of the footprint defined by the beam divergence angle. This resolution represents a practical

Table 1
Instrument specifications for Riegl VZ-4000 long-range TLS and Gamma Portable Radar Interferometer (GPRI-II).

	VZ-4000	GPRI-II
Range Resolution Δr	–	75 cm
Azimuth Angle Steps $\Delta \alpha$	0.0045°	0.1°
Angular Resolution	< 0.0005°	0.385°
Range Accuracy (at 150 m)	15 mm	–
Range Precision (at 150 m)	10 mm	–
Laser Beam Divergence ($1/e^2$)	0.15 mrad	–

compromise between scanning time and ensuring sufficiently dense sampling for the precise TCE. During each TLS scan, the faster data acquisition capability of the TRI allowed for the completion of 5 TRI scans in one set, resulting in a total of 70 (14x5) scans. Due to sporadic stability issues at the start of each set observed in previous measurement campaigns, the initial TRI scan of each set was omitted, resulting in 56 (14x4) observations. The position of the instruments remained unchanged throughout the observations.

The data acquisition for each target location required approximately 30 min. During this period, meteorological conditions remained relatively stable, with temperature fluctuations $<1°$. The estimated changes in the measured distances for all target locations, attributable to atmospheric refraction variations, were less than 2 mm. Given this minor effect and considering the precision of the instruments given in Table 1, the impact of atmospheric refraction was neglected in further analysis.

The target centers of both TLS and TRI datasets were extracted by the methods introduced in Sec. 2. The results of the precision analysis for both instruments are given in the following section.

3.2. TCE precision: results for TLS

The results of analyzing the TCE precision for the TLS are given in polar coordinates and summarized in Table 2. The precision estimates are calculated as 1σ standard deviation (STD), for the range σ_R, azimuth σ_{Az}, and elevation angle σ_{El} from 14 observations at three target locations at different distances (Fig. 6, left). We computed the polar coordinates as they are related to the genuine TLS-specific sensing dimensions and are easier to interpret and compare to the instrumental specifications. They are computed from the target centers $\mathbf{c}_{TLS}$ given in Cartesian coordinates. As a summarizing precision metric encompassing uncertainty of all 3 polar observations, $\bar{d}_{3D}$ represents the mean spatial distance of the individual target centers from the overall mean target center across all 14 point clouds per target location. The precisions are computed twice, once directly from the raw observation and once after preprocessing (marked as w/o and w/). First, we present the results without the preprocessing.

The precision of the range measurement exhibits sub-millimeter levels at closer ranges, decreasing to 1.4 mm at the furthest measured distance. This precision surpasses the instrument's specified precision of 10 mm at 150 m by an order of magnitude. This can be explained as several hundred points (500–800) are available for the TCE with the selected scanning resolution, allowing for a significant reduction of the range noise by averaging. The precision estimates σ_{Az} and σ_{El} amount several millidegrees, surpassing the angular resolution specified in Table 1 by 2–3 times (exception at Target B). Due to the lever arm effect over long ranges, this uncertainty is the predominant influence on the precision of the target center positioning, when considered in Euclidean space, amounting to several centimeters at the distances where the targets are located. The resulting $\bar{d}_{3D}$ is approximately 1/3 of the

footprint size, which varies with beam divergence from 180 mm at a distance of 1.2 km–345 mm at 2.3 km. The presented precision estimates are representative of the overall cumulative errors with the uncertainty stemming from the target center estimation approach, the setup stability, and any instrumental and environmental effects. Consequently, these estimates offer a realistic representation of the precision achievable in field conditions, and what can be expected during practical applications.

A closer examination of σ_{Az} for target B, which displayed a significantly larger standard deviation, revealed variability between the individual point clouds explainable by a rigid body motion, suggesting potential setup instabilities as the main contributing factor. Therefore, we assessed the possibility of using point cloud registration to mitigate this effect. For this, 13 subsequent point clouds are registered with a 3DOF-ICP, as introduced in Sec. 2.2.3, to the first one. We then repeated the process of TCE and calculated the same previously discussed statistical measures (Table 2, "w/" as "with pre-processing").

The overall 3d center precision $\bar{d}_{3D}$ is improved by up to a factor of 2 when introducing this pre-processing step, primarily due to the noticeable increase in the precision of elevation measurements. This confirms that the registration compensates for some of the systematic effects, having a positive influence on the 3d position quality. Therefore, we recommend acquiring multiple consecutive point clouds in the case of georeferencing tasks with low uncertainty demands and co-registering them before the TCE step (as outlined in Fig. 3). With the latter pre-processing, the TCE precision is on the level of 3–4.5 cm and is a bit higher than what was reported by (Schröder and Gaisecker, 2022). However, their dataset also included some targets at larger distances, hinting at a direct comparable performance.

These values are more than an order of magnitude smaller than the expected achievable TCE precision for TRI system based on the literature evidence (e.g. Caduff and Rieke-Zapp (2014)) Hence, these results confirm that the chosen 1-inch prism size provides sufficient TCE precision and is suitable for our application. Finally, the TCE uncertainty presented in Table 2 can be considered approximately stable over the investigated ranges, which simplifies the estimation of the expected georeferencing uncertainty due to the range independence. One alternative approach involves initially detecting the targets, followed by registering the point cloud over these target centers, particularly when the scene is not suitable for precise ICP registration. This method requires a sufficient number of well-placed targets with optimal geometry. However, investigating the optimal target placement and exploring the implications of subsequent matching processes fall beyond the scope of this work.

3.3. TCE precision: results for TRI

The comparable results for the TRI are summarized in Table 3, showing the estimated precision as the 1σ STD for the range σ_R, for the azimuth σ_{Az} and the mean 2d distance from the mean target center $\bar{d}_{2D}$, for the three test sites, with and without pre-processing. When
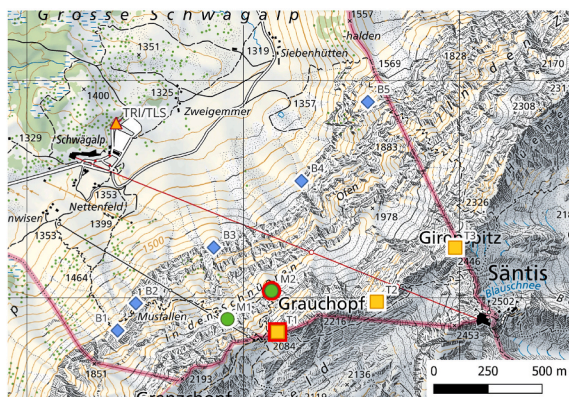
Table 2
Precision of the estimated target centers extracted from the TLS point clouds for three sites (A: 1.2 km, B: 1.5 km, C: 2.3 km) given in the TLS-specific sensing directions (range, azimuth and elevation angle); $\bar{d}_{3D}$ shows the mean spatial distance from the individual target centers from the overall mean target center across all point clouds ("w/o" - using the raw measurements without applying any point cloud pre-processing; "w/" - after point cloud registration by 3DOF-ICP).

Preproc	Site	σ_R (mm)	$\sigma_{Az}(°)$	$\sigma_{El}(°)$	$\bar{d}_{3D}$ (mm)
w/o	A	0.7	0.0016	0.0008	33.3
	B	0.8	0.0032	0.0013	106.7
	C	1.4	0.0011	0.0010	50.8
w/	A	1.2	0.0017	0.0008	39.5
	B	1.0	0.0018	0.0006	43.2
	C	1.3	0.0009	0.0005	37.0

Table 3
Estimated precision of the mmCR target centers extracted from the TRI images for the three different test sites: A, B, and C ("w/o" - using the raw measurements without applying any pre-processing; "w/" - after co-alignment of amplitude images).

Preproc	Site	σ_R (mm)	σ_{Az} (°)	$\bar{d}_{2D}$ (mm)
w/o	A	15.8	0.0116	140.2
	B	16.5	0.0094	158.5
	C	22.7	0.0102	246.8
w/	A	21.8	0.0099	123.7
	B	27.4	0.0085	134.5
	C	27.6	0.0093	222.4

considering the results based on raw observations without pre-processing, the range precision σ_R was on the order of 1–2 cm and showed a slight range dependency. However, these values are noticeably lower than the system's range resolution (Table 1) and the changes are small. Hence, for the sake of simplicity, the uncertainty can be considered as constant over distance. Unlike range precision, azimuth precision does not show any observable dependency on range. When σ_{Az} values are compared to the azimuth step size of 0.1°, as specified in Table 1, they are two orders of magnitude smaller than native azimuth resolution, demonstrating the effective sub-pixel precise TCE. Comparable to the TLS case, the 2d target precision $\overline{d}_{2D}$ in Euclidean space mainly depends on σ_{Az} and exhibits a noticeable rise with increasing range, attributable to the lever-arm effect.

With the inconsistency in azimuth precision across different target locations (e.g. between A and C vs. B) and no clear dependency on range, we assume potentially similar disturbances arising from the instability of the instrument setup as observed in the TLS data that could be explained by a rigid body motion. To investigate these effects, we deployed a similar data-driven registration strategy, where all the subsequent amplitude images are aligned to the first observation of the entire radar image stack as introduced in Sec. 2.2.3. The results are shown in Table 3 under the "w/" label. Similar to the TLS data, a small but noticeable decrease in the range precision is observed, accompanied by the simultaneous increase in the azimuth precision, signalizing some redistribution of errors. This drop in σ_R is likely due to a lack of distinct features well distributed in the range direction within the amplitude image. Consequently, image alignment is less precise in this direction compared to the azimuth direction. Yet, σ_R remains within 2–3 cm which is still noticeably smaller than the original TRI image resolution and is expected to be sufficient for precise georeferencing (again, values much smaller than the best TCE precision reported in the literature, as e.g. in Caduff and Rieke-Zapp (2014)). The observable improvements in the azimuth direction (11% on average) play a more relevant role in the overall 2d target position precision $\overline{d}_{2D}$, which amounts 1–2 dm after data pre-processing. Additional pre-processing of the raw data (before generating of the SLC), as suggested by Baffelli et al. (2018), could further improve the precision of the TCE. The results indicate that the developed approach enables the determination of a target center position with the precision equaling a fraction of the original SLC pixel size (2 orders of magnitude smaller), aligning with findings discussed by Balss et al. (2018). Finally, these results, together with the ones reported for TLS data, confirm that our 2nd design criterion for the mmCR was fulfilled (see Sec. 2.1).

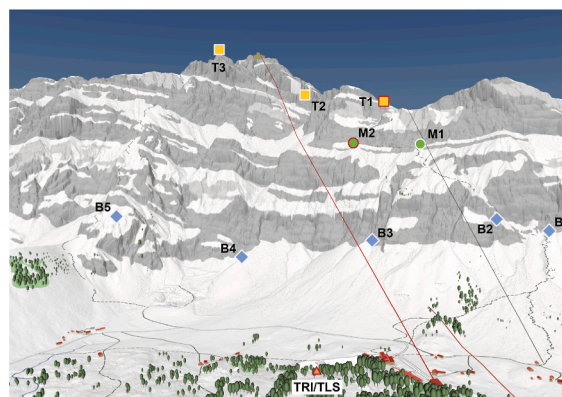### 3.4. Georeferencing uncertainty assessment: set-up

In our second experiment, we focus on evaluating the achievable georeferencing uncertainty using the proposed approach based on mmCRs as targets as introduced in Sec. 2.2.3. For this assessment, data was acquired at the Säntis north face, AR, Switzerland, where 10 mmCR targets were installed, as depicted in Fig. 7. The placement of these mmCR targets spanned distances ranging from 600 m to 2000 m and it covered the elevation angles from 8° to 38°, with height differences ranging from 130 m to 1100 m. The mmCR were set up on a surveying bolt, secured to bare rock, and aligned with a scope (as introduced in Sec. 2.1) towards the instrument position. This experiment setup represents a realistic proxy for a common geomonitoring setting.

We acquired 9 point clouds using Riegl VZ-4000 TLS scanner, which was mounted with a tilt of 10° on a custom mount placed on the ground. This special mount was needed to cover the highest features of the rock face with an elevation angle of 38°, as the scanner opening angle is ±30°. The scanning resolution was identical to the experiment in Sec. 3.1. One scan took approximately 60 min for a field of view of horz. 120° x vert. 40°. The TRI images were observed with the GPRI-II set on a heavy-duty tripod in proximity to the TLS instrument. In total, we acquired 37 SLC with 2-min intervals, with identical parameters as in the first experiment, although this time the antenna elevation was adjusted by 40° to point to the farthest point, in our case the mountain ridge, as recommended by the manufacturer. The atmospheric conditions were stable during the observations and within the expected range that can be encountered in practice.

3.5. Results: georeferencing

To evaluate the uncertainty of georeferencing with the proposed approach, we followed the workflow outlined in Sec. 2.2.3. We first registered all 9 of the collected point clouds with the ICP algorithm, ran the target detection and center estimation routine, and averaged the center coordinates of the corresponding targets. The TRI amplitude images were processed in a comparable fashion, following the workflow presented in Fig. 3, B. These averaged observations of 10 targets realized with both instruments served as a basis for georeferencing and evaluating the related uncertainty.

The uncertainty of georeferencing and the subsequent mapping uncertainty was evaluated in several ways. The first way was analyzing the discrepancy or a mismatch of the target coordinates between TRI and TLS data after georeferencing, i.e. estimating and applying coordinate transformations. The resulting coordinates are expressed as 2D Cartesian coordinates in a 2D TRI coordinate system (see Sec. 2.2.3). Ideally, the discrepancies between TRI and TLS datasets should tend towards 0 after

Fig. 7. The map (left) of the experiment location shows the instrument setup locations (orange triangle) and the distribution of 10 mmCRs, categorized into three groups based on their similar elevation angles (blue rhomboids, green circles, and yellow squares). The targets marked in red (M2 and T1) are shown to be outliers in the assessment. The corresponding 3d visualization is on the right. Basemap: © swisstopo. (For interpretation of the references to color in this figure legend, the reader is referred to the Web version of this article.)

the georeferencing. The deviations from this expectation are caused by the TCE uncertainty and any remaining systematic errors that were not resolved by the georeferencing equations. We summarize all discrepancies by computing the mean 2D Euclidian distance over all 10 targets, denoted as D_{2D}.

To justify the inclusion of the range offset parameter δ_r in our georeferencing equations in addition to the typically used 6DOF transformation (see Sec. 2.2.3 for details), we did georeferencing with and without δ_r and compared the D_{2D} values. The inclusion of range offset noticeably reduced the D_{2D} values from 1.27 to 0.18 m, highlighting its relevance. The δ_r value was significantly different from 0, amounting 5.6 m. The plausibility of the magnitude of this value was confirmed within the correspondence with the instrument manufacturer.

The computed D_{2D} value already provides the first insights into the achievable uncertainty of mapping TRI data onto TLS point clouds, facilitated by our georeferencing approach. It hints that we can achieve a mapping uncertainty in the order of a few decimeters. However, as each of the targets was directly used in georeferencing, the estimated mapping uncertainty could be overly optimistic. To acquire a more independent metric, we repeated the georeferencing procedure with only 9 targets using the leave-one-out cross-validation (LOOCV), see e.g. James et al. (2023), and computed the coordinate discrepancies (2D Euclidean distances) of the excluded targets. The median discrepancy of 25 cm indicates that the expected mapping uncertainty is indeed comparable to the precision of the TRI target center estimates (see Sec. 3.3). A median absolute deviation (MAD) of 7 cm further suggests that the mapping uncertainty is mostly consistent across georeferencing solutions realized with different target subsets.

These findings present a significant improvement, being an order of magnitude better than the results (1.77 m) reported by Caduff and Rieke-Zapp (2014) for the comparable target-based georeferencing (but with no automation). Moreover, the presented results are an order of magnitude better than the mapping uncertainty results (4.0 m) reported for the approaches relying on natural features, as e.g. shown by Schmid et al. (2023). Hence, our target-based georeferencing approach can be used in tasks demanding low mapping uncertainty and is likely to achieve superior performance relative to the approaches previously reported in the literature.

Upon examining the error distribution w. r.t the azimuth and elevation directions, as well as range, we did not identify any systematic patterns that would signalize the need for including any additional terms in the georeferencing equation. Consequently, we infer that the remaining errors are primarily of a random nature.

Although the low mapping uncertainty of TRI data into 3d space remains the primary goal of georeferencing, further exploring the uncertainty of the individual transformation parameters offers valuable insights as it can be used for estimating the mapping uncertainty beyond the observed scene. For that, we initially computed georeferencing results for all permutations of target combinations for groups ranging from 3 to 9 targets. This approach serves a dual purpose: it indicates the minimum number of targets required for reliable georeferencing, and it offers insights into the variability of transformation parameters w.r.t. the measurement configuration.

A preliminary analysis based on these reduced subsets of targets indicated that two targets (M2 and T1, as marked in Fig. 7) exhibited a D_{2D} more than three times higher than the MAD from the median of all targets, significantly skewing the results. Consequently, these targets were identified as outliers and were removed from the dataset for further analysis.

In Fig. 8 we present the MAD for the estimated values of each transformation parameter as a function of the number of targets used for georeferencing. As expected, the MAD reduces by adding more targets for all parameters. It can be observed that already the configurations with five targets allow for translation parameters to be estimated with an uncertainty lower than 1 m, and rotation parameters with an uncertainty lower than 0.1°. For comparison, this is several times smaller
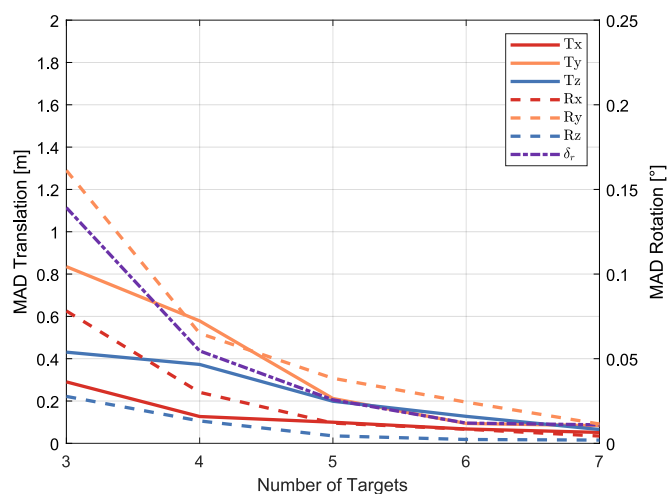

Fig. 8. The Median Absolute Deviation (MAD) for each transformation parameter, plotted against the number of targets used for the georeferencing (solid lines: translation parameters, dashed lines: rotation parameters).

parameter variability than the one reported for the purely data-driven approach reported in Schmid et al. (2023). However, it's important to note that for the latter, the distribution of features is much bigger and more consistent across different realizations. Hence, the estimates are less independent and the comparison is not completely equitable. A more thorough evaluation is necessary to accurately assess and compare the parameter uncertainties of both methodologies. Hence, this is just the first indication of the relative performance differences between the state-of-the-art data-driven and target-based georeferencing approaches considering the uncertainty of the estimated transformation parameters.

It is worth noting that the variability of the parameters is significantly affected by the spatial distribution of targets in the dataset. Hence, although the quantities presented for this particular dataset hint at the achievable parameter quality, they are likely not fully generalizable, and the final parameter quality will depend on the geometry of the targets of each experiment setup.

We can further observe in Fig. 8 that the parameters associated with the y-axis direction (T_y, R_y and δ_r) exhibit a higher MAD, especially when only a few targets (<5) are used. This is likely caused by the limited spread of targets along the line of sight, which reduces the controllability of these parameters, primarily due to the topographic setting of the observed scenery. Our assumption is corroborated by significant correlations between T_y and δ_r ($R^2 = -0.96$, Pearson's linear correlation coefficient) and T_y and R_y($R^2 = -0.60$), indicating that these parameters are not distinctly separable and that they reciprocally compensate for changes in parameter values. Consequently, the elevated MAD for these parameters likely has a small impact on the mapping uncertainty due to this mutual compensation.

To confirm that, we computed the third metric for evaluating the mapping uncertainty that represents the impact of the variability of transformation parameters on the mapping of the target centers. For that, in Fig. 9 we show the mean D_{2D} of each mmCR (and their mean) as a function of the number of targets. These D_{2D} values are computed using all sets of transformation parameters also used for computing the values presented in Fig. 8. The mean D_{2D} values (black dashed line in Fig. 9) tend to be smaller than the uncertainty of some of the individual transformation parameters (e.g. T_y and δ_r in Fig. 8). This observation corroborates the statement about mutual compensation of parameter variability between the correlated parameters and provides the final confirmation that the expected mapping uncertainty is in the order of a few decimeters.
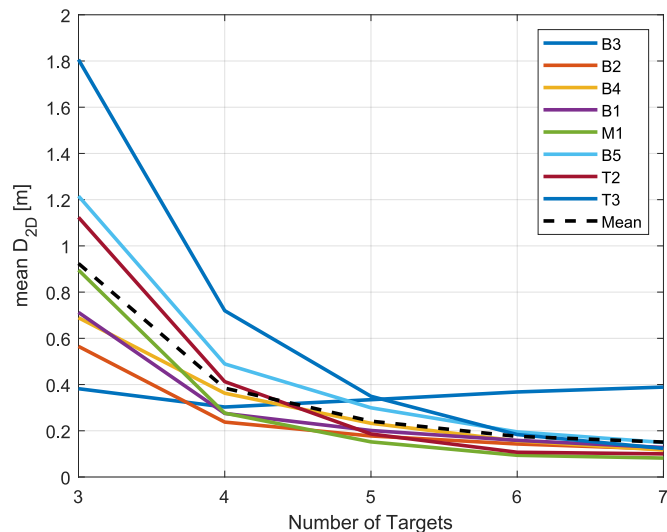
Fig. 9. Effect of transformation parameter variability on referenced targets, displayed as mean D_{2D} for each installed mmCR and their mean.

4. Conclusion

We have developed a multi-modal corner reflector (mmCR) for georeferencing TRI images with 3d TLS point clouds. The proposed mmCR is lightweight and portable, allowing easy implementation in challenging or hard-to-reach terrain, and it can be used to materialize a common point in TRI/TLS datasets with the precision of the target center estimation reaching 1–2 cm for TLS and 1–2 dm for TRI, demonstrated up to a range of 2.3 km.

Additionally, we present a fully automated data processing pipeline that leverages the detected target centers to facilitate georeferencing with low uncertainty and that allows comprehensive quality assessments. In our experiments we achieved an average mapping uncertainty of 18.8 cm (mean 2d positional error of target centers between TLS and TRI after the georeferencing), demonstrating the pipeline's efficacy in a realistic geomonitoring setting. Such a target-based georeferencing workflow provides the means for reliable and precise georeferencing in scenarios where manual detection of salient natural features poses a challenge. The main requirement is the accessibility of the locations where the mmCR should be installed.

The potential applications of the developed mmCRs extend beyond georeferencing. They can serve as a tool for more rigorously evaluating the mapping uncertainty achieved by different georeferencing approaches, providing the means for their direct comparison and benchmarking. Moreover, they can also be used to generate ground truth data for improving the existing data-driven approaches for TRI georeferencing, such as the one presented in Schmid et al. (2023). Additionally, such ground truth can be used to validate the suitability of applying advanced, tie-point-free georeferencing methods developed for spaceborne SAR, as the one presented in Frey et al. (2013), to TRI data. This would also advance and enable high-precision georeferencing using data-driven approaches, where the installation of in-situ targets is prohibitively dangerous.

Finally, apart from georeferencing and mapping quality analysis, the mmCR could also be used for atmospheric phase screen correction, which can be applied for monitoring applications with TRI, as e.g. explained by (Iannini and Monti Guarnieri, 2011). A future study will explore the efficacy of precisely aligned surface models for advanced Atmospheric Phase Correction (APC), considering surface topography.

CRediT authorship contribution statement

Lorenz Schmid: Writing – original draft, Visualization, Validation,

Software, Project administration, Methodology, Investigation, Formal analysis, Data curation, Conceptualization. **Tomislav Medic:** Writing – review & editing, Writing – original draft, Validation, Supervision, Methodology, Investigation, Conceptualization. **Othmar Frey:** Writing – review & editing, Supervision, Conceptualization. **Andreas Wieser:** Writing – review & editing, Supervision, Methodology, Funding acquisition, Conceptualization.

Declaration of competing interest

Acknowledgments

References

Agliardi, F., Crosta, G.B., Sosio, R., Rivolta, C., Mannucci, G., 2013. In situ and remote long term real-time monitoring of a large alpine rock slide. In: Margottini, C., Canuti, P., Sassa, K. (Eds.), Landslide Science and Practice. Springer Berlin Heidelberg, Berlin, Heidelberg, pp. 415–421.

Baffelli, S., Frey, O., Werner, C., Hajnsek, I., 2018. Polarimetric calibration of the ku-band advanced polarimetric radar interferometer. IEEE Trans. Geosci. Rem. Sens. 56 (4), 2295–2311.

Balss, U., Gisinger, C., Eineder, M., Breit, H., Schubert, A., Small, D., 2018. Survey protocol for geometric SAR sensor analysis. Tech. rep.

Besl, P., McKay, N.D., 1992. A method for registration of 3-D shapes. IEEE Trans. Pattern Anal. Mach. Intell. 14 (2), 239–256.

Caduff, R., Rieke-Zapp, D., 2014. Registration and visualisation of deformation maps from terrestrial radar interferometry using photogrammetry and structure from motion. Photogramm. Rec. 29 (146), 167–186.

Caduff, R., Schlunegger, F., Kos, A., Wiesmann, A., 2015. A review of terrestrial radar interferometry for measuring surface change in the geosciences. Earth Surf. Process. Landforms 40 (2), 208–228.

Crosta, G.B., Agliardi, F., 2003. A methodology for physically based rockfall hazard assessment. Nat. Hazards Earth Syst. Sci. 3 (5), 407–422.

Czikhardt, R., Van Der Marel, H., Papco, J., 2021. GECORIS: an open-source toolbox for analyzing time series of corner reflectors in InSAR geodesy. Rem. Sens. 13 (5), 926.

Eberhardt, E., Watson, A.D., Loew, S., 2008. Improving the Interpretation of Slope Monitoring and Early Warning Data through Better Understanding of Complex Deep-Seated Landslide Failure Mechanisms.

Freeman, A., 1992. SAR calibration: an overview. IEEE Trans. Geosci. Rem. Sens. 30 (6), 1107–1121.

Frey, O., Santoro, M., Werner, C.L., Wegmuller, U., 2013. DEM-based SAR pixel-area estimation for enhanced geocoding refinement and radiometric normalization. Geosci. Rem. Sens. Lett. IEEE 10 (1), 48–52.

Frodella, W., Ciampalini, A., Gigli, G., Lombardi, L., Raspini, F., Nocentini, M., Scardigli, C., Casagli, N., 2016. Synergic use of satellite and ground based remote sensing methods for monitoring the San Leo rock cliff (Northern Italy). Geomorphology 264, 80–94.

Garthwaite, M., 2017. On the design of radar corner reflectors for deformation monitoring in multi-frequency InSAR. Rem. Sens. 9 (7), 648.

Garthwaite, M., Nancarrow, S., Hislop, A., Thankappan, M., Dawson, J., Lawrie, S., 2015. The Design of Radar Corner Reflectors for the Australian Geophysical Observing System: a single design suitable for InSAR deformation monitoring and SAR calibration at multiple microwave frequency bands. Tech. rep., Geoscience Australia.

Guizar-Sicairos, M., Thurman, S.T., Fienup, J.R., 2008. Efficient subpixel image registration algorithms. Opt Lett. 33 (2), 156.

Iannini, L., Monti Guarnieri, A., 2011. Atmospheric phase screen in ground-based radar: statistics and compensation. Geosci. Rem. Sens. Lett. IEEE 8 (3), 537–541.

James, G., Witten, D., Hastie, T., Tibshirani, R., Taylor, J., 2023. An Introduction to Statistical Learning: with Applications in Python. Springer Texts in Statistics. Springer International Publishing, Cham.

Janßen, J., Kuhlmann, H., Holst, C., 2021. Assessing the temporal stability of terrestrial laser scanners during long-term measurements. In: Kopáčik, A., Kyrinovič, P., Erdélyi, J., Paar, R., Marendić, A. (Eds.), Contributions to International Conferences on Engineering Surveying. Springer International Publishing, Cham, pp. 69–84.

Kos, A., Conforti, D., Tompkinson, W., Strozzi, T., Wiesmann, A., Lunghi, A., 2010. Integration of Terrestrial LiDAR and Ground-Based Radar Interferometry for Monitoring Rock Slopes Following Blast Mitigation.

Lagarias, J.C., Reeds, J.A., Wright, M.H., Wright, P.E., 1998. Convergence properties of the Nelder–Mead simplex method in low dimensions. SIAM J. Optim. 9 (1), 112–147.

Li, H.-b., Yang, X.-g., Sun, H.-l, Qi, S.-c., Zhou, J.-w., 2019. Monitoring of displacement evolution during the pre-failure stage of a rock block using ground-based radar interferometry. Landslides 16 (9), 1721–1730.

Luzi, G., Pieraccini, M., Mecatti, D., Noferini, L., Guidi, G., Moia, F., Atzeni, C., 2004. Ground-based radar interferometry for landslides monitoring: atmospheric and instrumental decorrelation sources on experimental data. IEEE Trans. Geosci. Rem. Sens. 42 (11), 2454–2466.

Monserrat, O., Crosetto, M., Luzi, G., 2014. A review of ground-based SAR interferometry for deformation measurement. ISPRS J. Photogrammetry Remote Sens. 93, 40–48.

Nathanson, F.E., O'Reilly, P.J., Cohen, M.N., 2004. Radar Design Principles: Signal Processing and the Environment, second ed. Scitech Publ, Raleigh, NC.

Noferini, L., Pieraccini, M., Luzi, G., Mecatti, D., Macaluso, G., Atzeni, C., 2006. Ground-based radar interferometry for terrain mapping. In: 2006 IEEE International Symposium on Geoscience and Remote Sensing. IEEE, Denver, CO, USA, pp. 2569–2572.

Pesci, A., Teza, G., 2008. Terrestrial laser scanner and retro-reflective targets: an experiment for anomalous effects investigation. Int. J. Rem. Sens. 29 (19), 5749–5765.

Pieraccini, M., Miccinesi, L., 2019. Ground-based radar interferometry: a bibliographic review. Rem. Sens. 11 (9), 1029.

Rebmeister, M., Auer, S., Schenk, A., Hinz, S., 2022. Geocoding of ground-based SAR data for infrastructure objects using the Maximum A Posteriori estimation and ray-tracing. ISPRS J. Photogrammetry Remote Sens. 189, 110–127.

Reshetyuk, Y., 2009. Self-Calibration and Direct Georeferencing in Terrestrial Laser Scanning. Arkitektur och samhällsbyggnad, Kungliga Tekniska högskolan, Stockholm.

Rossi, M., Sarro, R., Reichenbach, P., Mateos, R.M., 2021. Probabilistic identification of rockfall source areas at regional scale in El Hierro (Canary Islands, Spain). Geomorphology 381, 107661.

Ruck, G.T. (Ed.), 1970. Radar Cross Section Handbook, vol. 2. Plenum Press, New York, NY.

Schmid, L., Medic, T., Collins, B.D., Meier, L., Wieser, A., 2023. Georeferencing of terrestrial radar images in geomonitoring using kernel correlation. Int. J. Rem. Sens. 44 (21), 6736–6761.

Schröder, D., Anders, K., Winiwarter, L., Wujanz, D., 2022. Permanent terrestrial LiDAR monitoring in mining, natural hazard prevention and infrastructure protection – chances, risks, and challenges: a case study of a rockfall in Tyrol, Austria. In: Proceedings of the 5th Joint International Symposium on Deformation Monitoring - JISDM 2022. Editorial de la Universitat Politècnica de València.

Schröder, D., Gaisecker, T., 2022. RIEGL V-Line Scanners for Permanent Monitoring Applications and Integration Capabilities into Customers Risk Management.

Strozzi, T., Werner, C., Wiesmann, A., Wegmuller, U., 2012. Topography mapping with a portable real-aperture radar interferometer. Geosci. Rem. Sens. Lett. IEEE 9 (2), 277–281.

Ugray, Z., Lasdon, L., Plummer, J., Glover, F., Kelly, J., Marti, R., 2006. Scatter search and local nlp solvers: a multistart framework for global optimization. SSRN Electron. J.

Werner, C., Wiesmann, A., Strozzi, T., Kos, A., Caduff, R., Wegmüller, U., 2012. The GPRI multi-mode differential interferometric radar for ground-based observations. In: Synthetic Aperture Radar, 2012. EUSAR. 9th European Conference On. IEEE, Nürnberg, Germany, pp. 304–307.

Wilkes, P., Lau, A., Disney, M., Calders, K., Burt, A., Gonzalez de Tanago, J., Bartholomeus, H., Brede, B., Herold, M., 2017. Data acquisition considerations for Terrestrial Laser Scanning of forest plots. Rem. Sens. Environ. 196, 140–153.

Winiwarter, L., Anders, K., Czerwonka-Schröder, D., Höfle, B., 2023. Full four-dimensional change analysis of topographic point cloud time series using Kalman filtering. Earth Surf. Dyn. 11 (4), 593–613.

Wujanz, D., Neitzel, F., Hebel, H.P., Linke, J., Busch, W., 2013. Terrestrial radar and laser scanning for deformation monitoring: first steps towards assisted radar scanning. ISPRS Annals of the Photogrammetry. Remote Sens. Spatial Inf. Sci. II-5 (W2), 325–330.

Zheng, X., Yang, X., Ma, H., Ren, G., Zhang, K., Yang, F., Li, C., 2018. Integrated ground-based SAR interferometry, terrestrial laser scanner, and corner reflector deformation experiments. Sensors 18 (12), 4401.